A Scalable High-Throughput Isoelectric Fractionation Platform for Extracellular Nanocarriers: Comprehensive and Bias-Free Isolation of Ribonucleoproteins from Plasma, Urine, and Saliva

Himani Sharma[1], Vivek Yadav[1], Crislyn D'Souza-Schorey[3,4], David B. Go[1,2], Satyajyoti Senapati[1*], Hsueh-Chia Chang[1,2,3*]

[1] Department of Chemical and Biomolecular Engineering, University of Notre Dame, Notre Dame, IN, 46556, USA.

[2] Department of Aerospace and Mechanical Engineering, University of Notre Dame, Notre Dame, IN, 46556, USA.

[3] Harper Cancer Research Institute, University of Notre Dame, Notre Dame, IN, 46556, USA.

[4] Department of Biological Sciences, University of Notre Dame, Notre Dame, IN 46556, USA.

* corresponding author email: hchang@nd.edu and ssenapat@nd.edu

1. Supplementary Figures:

- Supplementary Figure 1: Water splitting module for pH gradient generation chip.
- Supplementary Figure 2: Schematics for the Finite Element simulation.
- Supplementary Figure 3: Separation chip optimization using 50 nm Carboxylated and aminated polystyrene nanoparticles.
- Supplementary Figure 4: Agarose Gel electrophoresis of the labeled HDL and LDL.
- Supplementary Figure 5: Preliminary experiments for parameter optimization for HDL and LDL.
- Supplementary Figure 6: Experimental setup for fractionation of HDL and LDL.
- Supplementary Figure 7: Optimization of the IEF separation of a mixture of HDL and RNP.
- Supplementary Figure 8: Fractionation of HDL and RNP mixture and gel electrophoresis.
- Supplementary Figure 9: The agarose gel electrophoresis of tagged HDL, LDL, RNP and commercial EVs.
- Supplementary Figure 10: Separation of LDL and EVs mixture in the separation chip under a very high-resolution pH gradient.
- Supplementary Figure 11: Recovery and purity data for binary fractionation of nanocarriers.
- Supplementary Figure 12: Graphical user interface for the *auto-CIF analyzer*.
- Supplementary Figure 13: *auto CIF analyzer* platform for fractionating HDL and LDL mixture.
- Supplementary Figure 14: Solidworks model and the 3D printed separation device.
- Supplementary Figure 15: Histograms of the Red, Green and Blue intensities of an image of a pH reference chart corresponding to different pH.
- Supplementary Figure 16: Histograms of the Red, Green and Blue intensities of images (shown in Figure 4f) corresponding to different pH for 3D printed chip.
- Supplementary Figure 17: Results of image segmentation module for xurography and 3D printed chips
- Supplementary Figure 18: Star topological configuration with pH gradient chip being the central node and different separation chips acting as connected nodes.
- Supplementary Figure 19: Yield and purity of RNP fractionation across various biofluids to demonstrate inter-day and intra-day performance of CIF.
- Supplementary Figure 20: Bradford assay results for HDL and LDL after incubation in different pH.
- Supplementary Figure 21: Cholesterol assay results for HDL and LDL after incubation in different pH.
- Supplementary Figure 22: RT qPCR results for mir21 after incubation in different pH.

- Supplementary Figure 23: TEM images of commercial EVs after incubation in different pH.
- Supplementary Figure 24: Simulated pH profiles to depict insensitivity of linear pH gradient to flow.

2. Supplementary Notes:

- Supplementary Note 1: pH Gradient Chip.
- Supplementary Note 2: Theoretical explanation of pH profile.
- Supplementary Note 3: Mathematical calculation of linear pH profile in both trapezoidal and straight channels.
- Supplementary Note 4: Insensitivity of linear pH gradient to flow.
- Supplementary Note 5: Optimized conditions for separating HDL and LDL.
- Supplementary Note 6: Optimized conditions for carboxylated and aminated latex particles in the separation chip.
- Supplementary Note 7: Optimized conditions for separating RNP and HDL.
- Supplementary Note 8: Use of *auto-CIF analyzer* for 3D printed CIF microfluidic chip.
- Supplementary Note 9: Image Segmentation Module and pH Detection Module of auto-CIF analyzer.
- Supplementary Note 10: On-chip gel electrophoresis and gel electrophoresis experimental details.

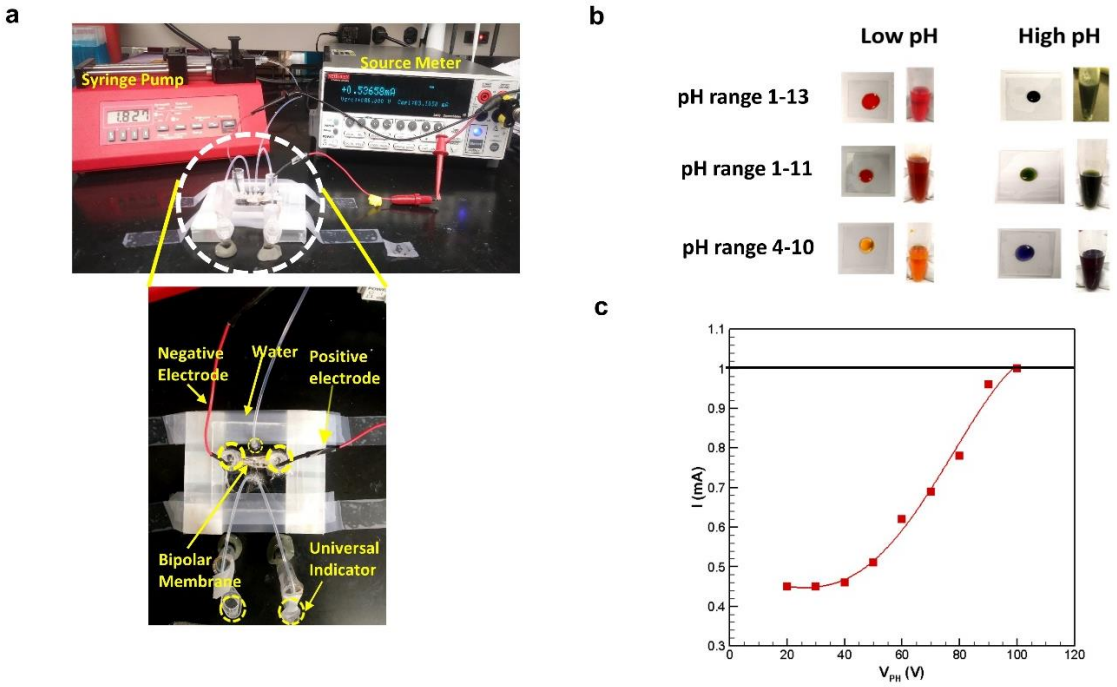

Supplementary Figure 1: a) Image of the experimental setup for testing water splitting module of pH gradient generation chip. The inset is a top view showing the water inlet and two electrode reservoirs for the bipolar membranes. **b)** pH analysis of the collected samples in microcentrifuge tubes from two different outlets as shown in *(a)* under different conditions of voltage bias **c)** Measured *I-V* characteristics of bipolar membrane depicting a significant increase in ion current at elevated voltages due to excessive hydroxide and hydronium ion generation by water splitting.

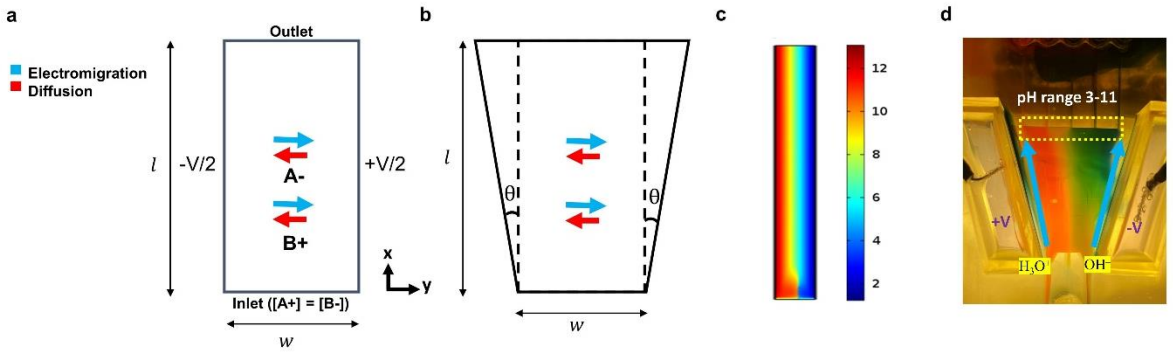

Supplementary Figure 2: Schematics for the FEM simulation setup for **a)** straight and **b)** trapezoidal geometry with an inlet width of *w*, length *l* and trapezoidal angle (θ). **c)** Surface plot of the pH profile for a straight channel obtained from FEM simulation. **d)** The pH profile obtained in the trapezoidal channel of the 3D printed chip.

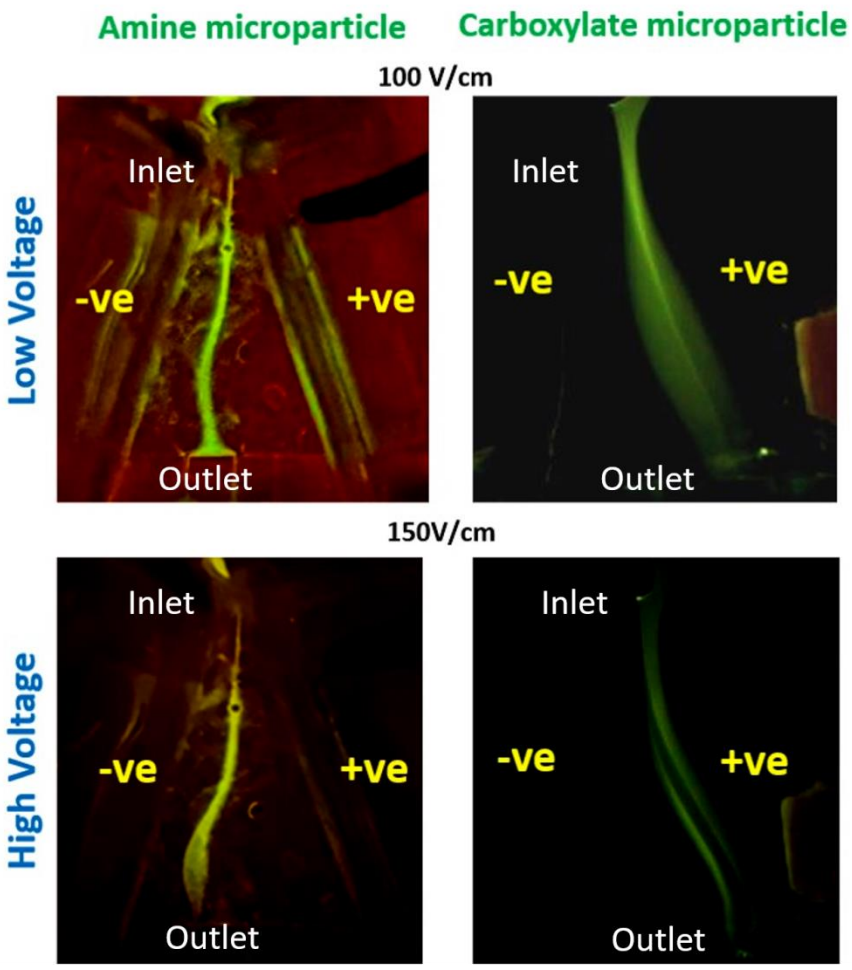

Supplementary Figure 3: Separation chip optimization using 50 nm carboxylated and aminated polystyrene nanoparticles. *Top row:* The deflection of aminated (left) and carboxylated (right) nanoparticles under a potential bias of 100V. *Bottom row:* Increased deflection of aminated (left) and carboxylated (right) nanoparticles under a higher potential of 150V.

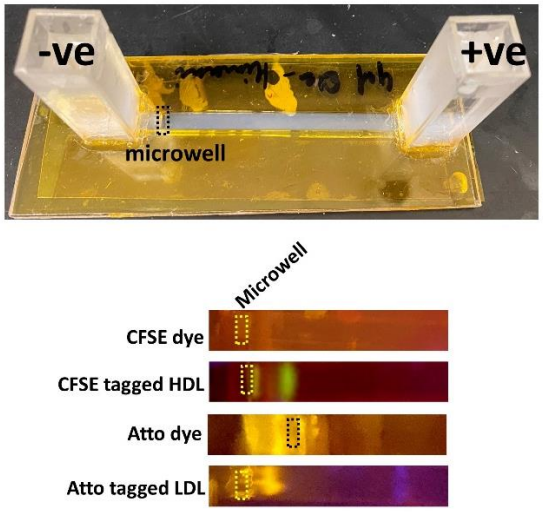

Supplementary Figure 4: Agarose Gel electrophoresis of the labeled HDL and LDL. *Top:* An image of the agarose gel electrophoresis chip. *Bottom:* Agarose gel (2% w/v) electrophoresis of the pure CFSE dye, CFSE labelled HDL, pure Atto dye and Atto dye labelled LDL. The dashed rectangular mark at the top indicates the position of the loading wells. The gel electrophoresis indicates efficient labelling of the LLPs with both LLPs moving towards the negative potentials. The CFSE dye is not fluorescent by itself and the Atto dye moves towards the positive potential.

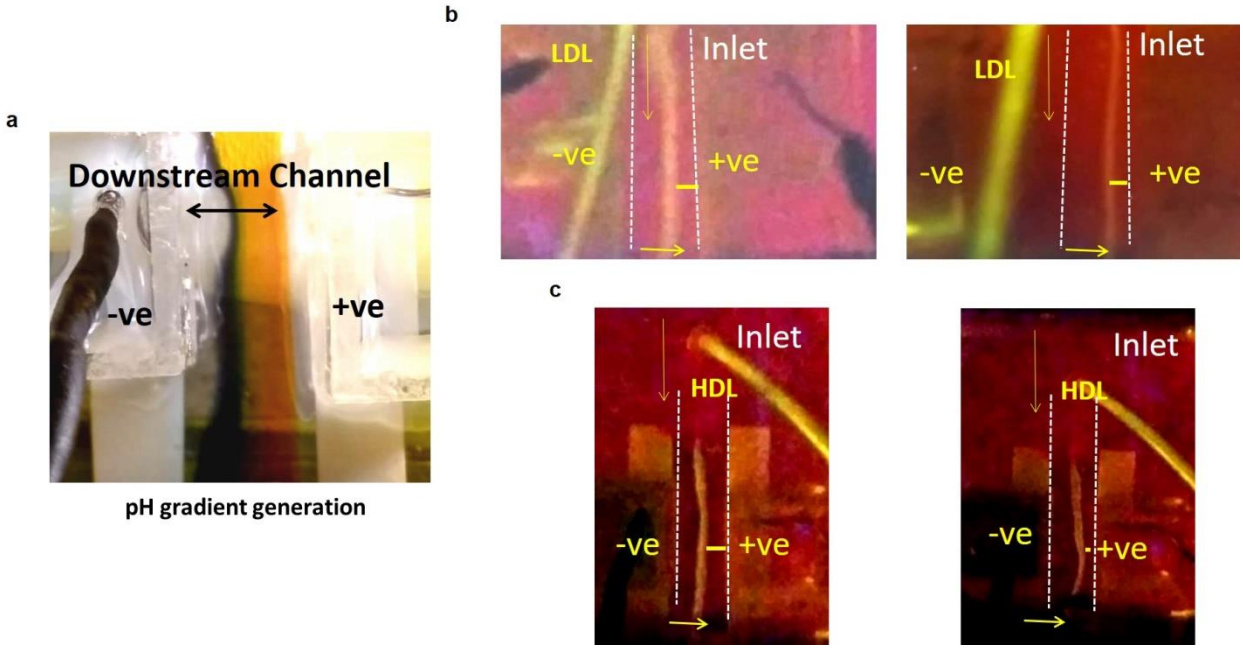

Supplementary Figure 5: Preliminary experiments for parameter optimization for IEF of HDL and LDL **a)** A chip for pH gradient generation with a pH of range 1-13. **b)** The deflection of labelled LDL in the chip under a voltage bias of 100V (left image) and 150V (right image). **c)** The deflection of labelled HDL in the chip under a voltage bias of 100V (left image) and 150V (right image).

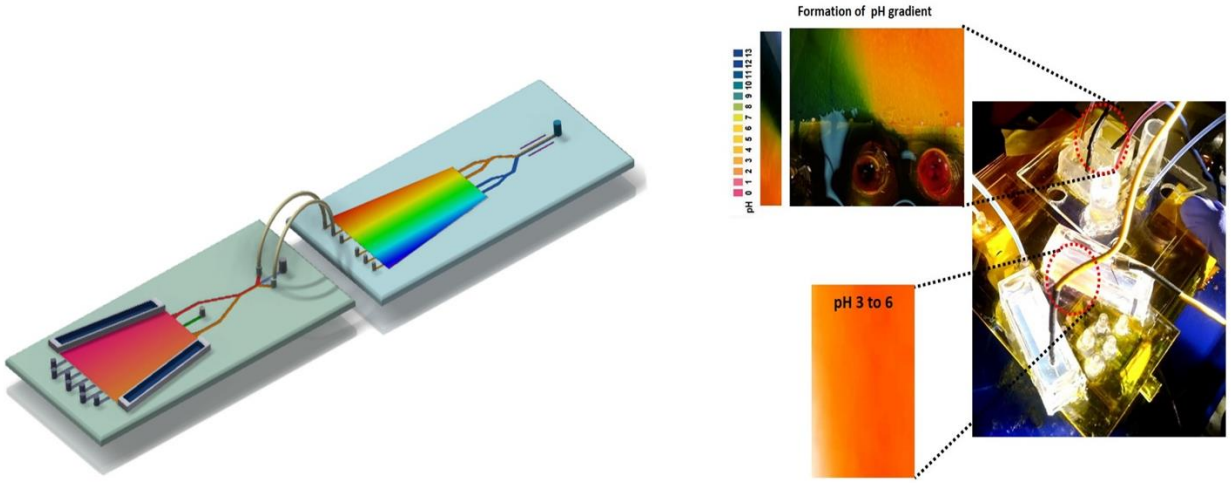

Supplementary Figure 6: *Left:* Schematics of the experiment for the separation of HDL and LDL mixture. A pH gradient generation chip produces a wide pH (2-11) and a selective pH (3-6) is transferred downstream into the separation chip. *Right:* The experimental images of the devices connected in a continuous manner depicting the transfer of a pH (3-6) downstream to a separation chip. *Right (Top side)*: Inset of the formation of pH gradient in the pH gradient chip and the transferred pH (range 3-6)

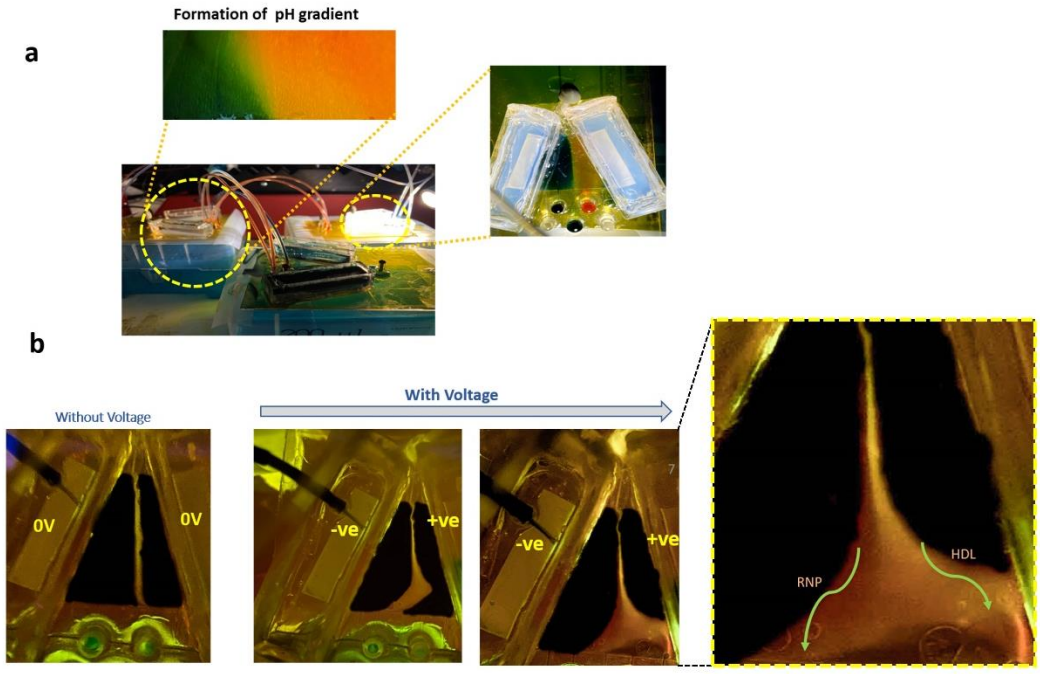

Supplementary Figure 7: Optimization of the IEF separation of a mixture of pure HDL and RNP. **a)** Left: Schematics of the experimental procedure in which a pH of 2-10 is transferred downstream from the pH generation chip to the separation chip. Right: Experimental images of the device working in continuous manner with image snapshots of the pH profile in the pH gradient chip and separation chip. **b)** As voltage is applied across the chip, the bioanalytes start to separate into two different streams till it reaches their isoelectric point. Two images show the movement of RNP and HDL towards correct potentials. A zoomed version of the last image shows the broad band of HDL and RNP.

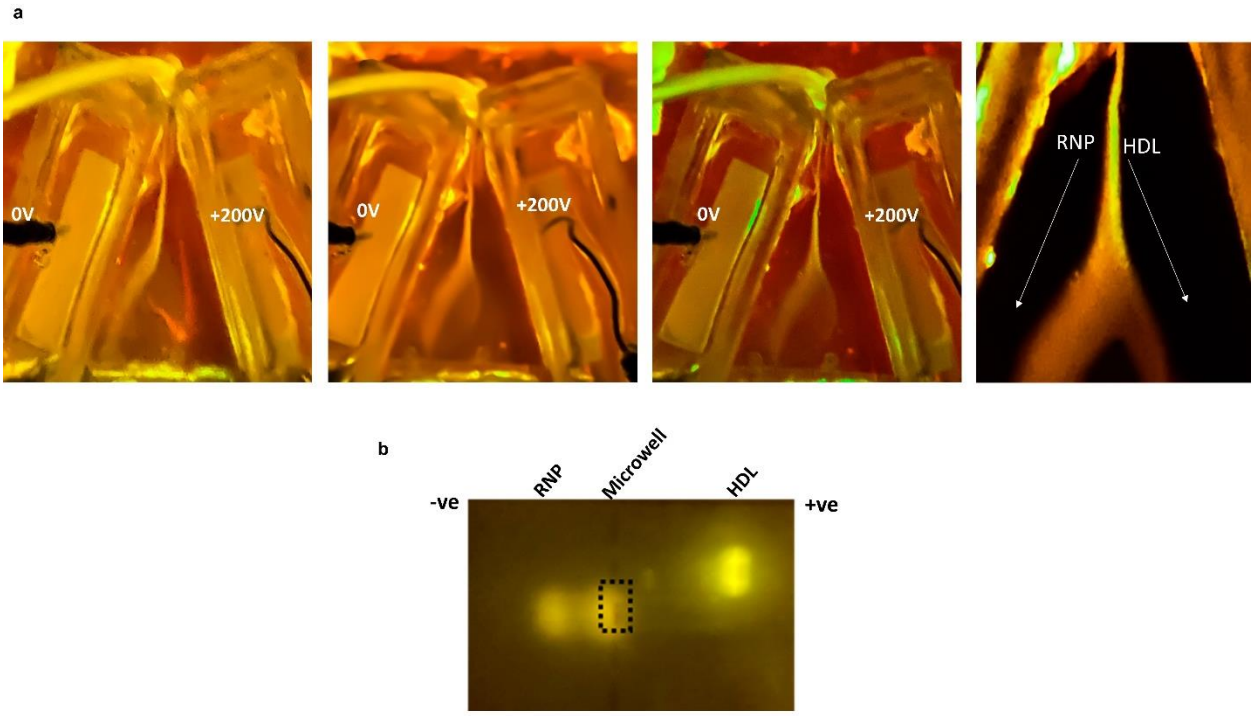

Supplementary Figure 8: a) Sequential images of the separation of HDL and RNP mixture in the separation chip. When 200V is applied, the HDL is deflected towards the positive electrode while the RNP is deflected towards the negative electrode and eventually two distinct streams are observed (shown in the last image). **b)** Gel electrophoresis of the collected HDL and RNP from their respective outlets show distinct bands of HDL and RNP without any significant cross-contamination.

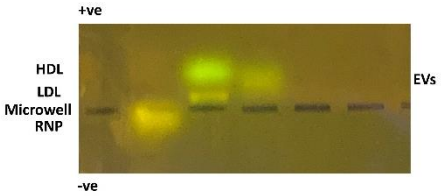

Supplementary Figure 9: The agarose (2% w/v) gel electrophoresis of tagged HDL, LDL, RNP and commercial EVs.

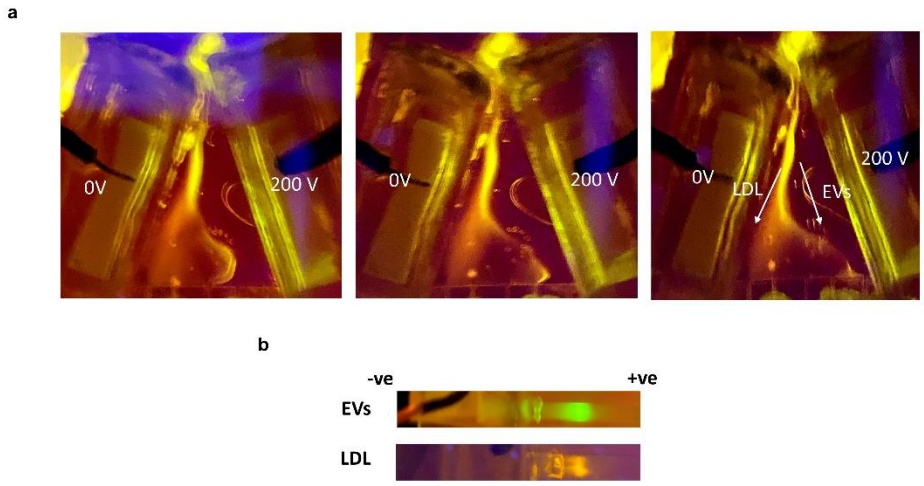

Supplementary Figure 10: a) Sequential images of the separation of LDL and EVs mixture in the separation chip under a very high-resolution pH gradient. The LDL is deflected towards the negative electrode and EVs are deflected towards the positive electrode. **b)** On chip gel electrophoresis experiments of EVs and LDL from the different outlets showing negligible cross-contamination.

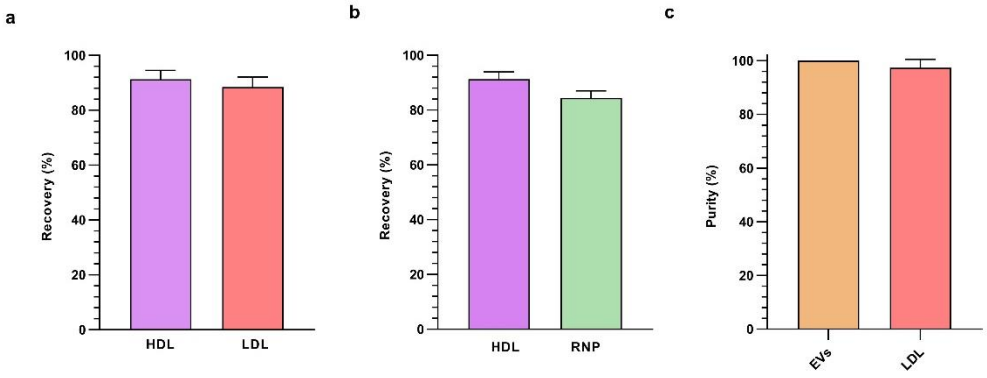

Supplementary Figure 11: a) Recovery of HDL and LDL from the CIF (n = 5). The data shows recovery of 91.33 ± 3.22% and 88.48 ± 3.62% recovery of pure HDL and LDL respectively from the mixture **b)** Recovery of HDL and RNP from the separation chip (n = 5). The data shows 91.26 ± 2.71% and 84.48 ± 2.59% recovery of pure HDL and pure RNP respectively from the mixture **c)** The purity of the mixture fractionation at the EVs outlet was evaluated to be 99.99997 ± 5.77×10^{-6} % whereas at the LDL outlet was evaluated to be 97.32567 ± 3.19564% (n = 4).

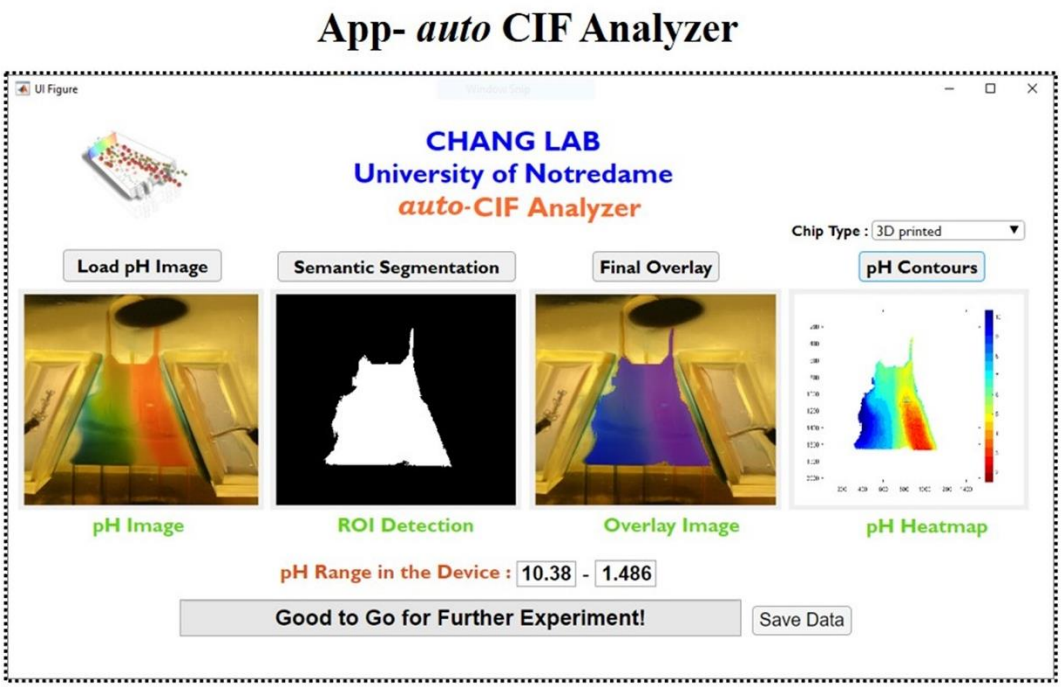

Supplementary Figure 12: Screenshot of the graphical user interface for the *auto-CIF analyzer* MATLAB® application that loads a colorimetric image taken from a smartphone image, identifies the ROI using machine learning, generates a segmentation mask, overlays the original image with the segmentation mask and generates the pH profile depending upon the chip type.

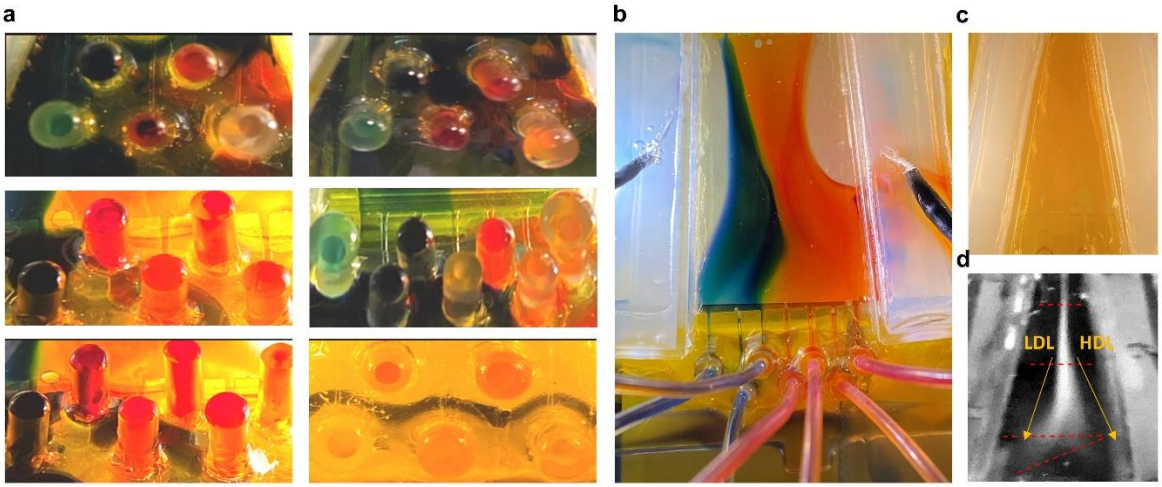

Supplementary Figure 13: a) A series of experimental images depicting different colors of pH dye in different outlets (5 and 7 outlets) with different pH generation chips. The colors at the outlet appear dark reddish/pinkish (acidic pH) or dark blue/ black (basic pH). This obscures user judgement regarding the pH value coming from each outlet. An appropriate way will be to use an *auto CIF analyzer* platform to determine the pH value in the pH generation trapezoidal channel itself. **b)** A snapshot of the pH generation chip generating a coarse and linear pH gradient. **c)** Separation chip image after transferring solution from outlet 3 and outlet 4 (outlet number starts from right to left) from the pH generation chip. **d)** Processed fluorescence image depicting clear separation of HDL and LDL in the separation chip. The red lines indicate the spatial locations which are used to draw line intensity plots in Figure 4l.

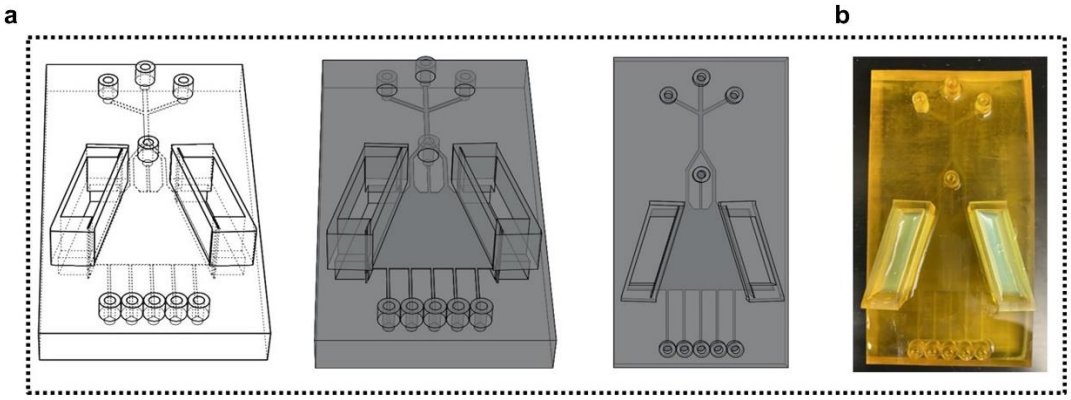

Separation Figure 14: a) Solidworks model of the 3D printed device in isometric wireframe mode and in solid isometric views. b) 3D printed device made by a commercial vendor (BMF, USA).

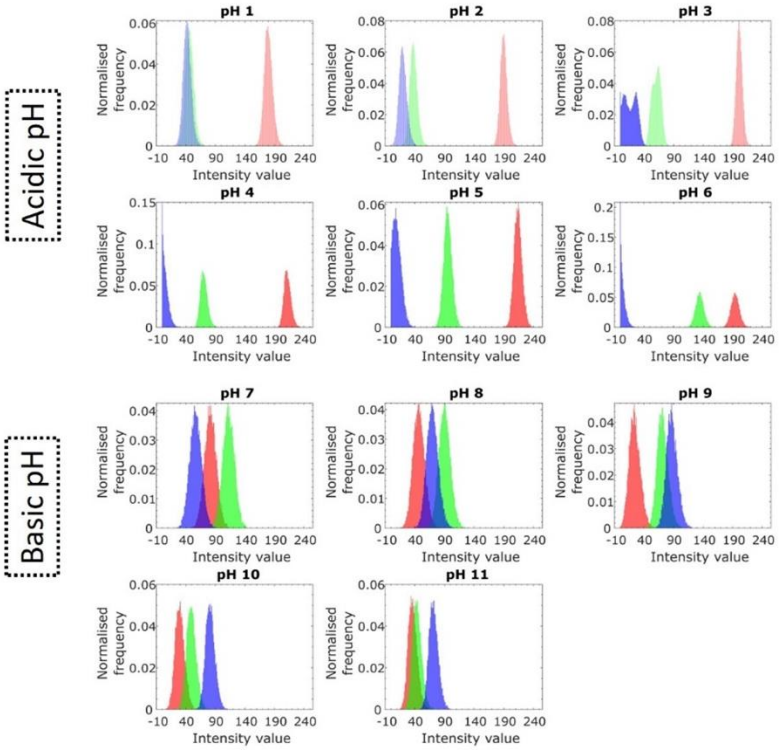

Supplementary Figure 15: Histograms of the Red, Green and Blue intensities of an image of a pH reference chart corresponding to different pH. The digital image was taken by a smartphone of the pH reference chart (Hydrion One Drop Indicator Solution Kit 1-11m, level7chemical.com) shown in Figure 4g.

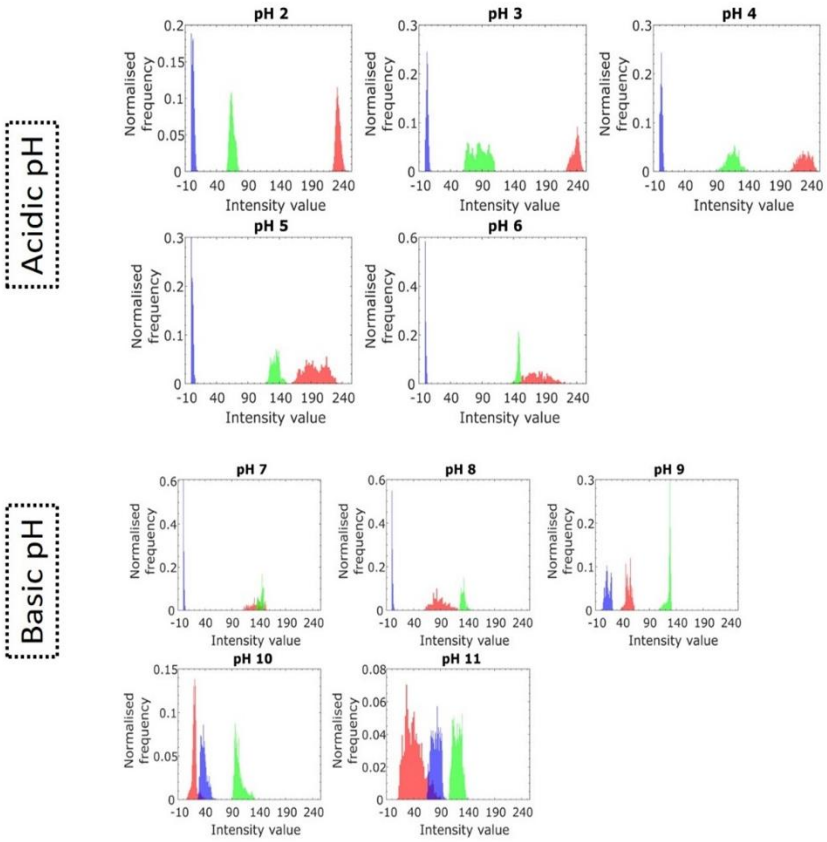

Supplementary Figure 16: Histograms of the Red, Green and Blue intensities of images (shown in Figure 4f) corresponding to different pH for 3D printed chip.

a

3D Print Device

	True Positive	False Positive
True	1.83E+07	1.18E+06
False	1.49E+06	1.08E+08
	False Negative	True Negative

b

Xurography Device

	True Positive	False Positive
True	6.60E+07	7.14E+06
False	4.44E+06	1.89E+08
	False Negative	True Negative

Supplementary Figure 17: Table containing the raw data of true positive, true negative, false positive and false negative values obtained by summation of all pixels in the test images of **a)** 3D printed and **b)** xurography-based chip.

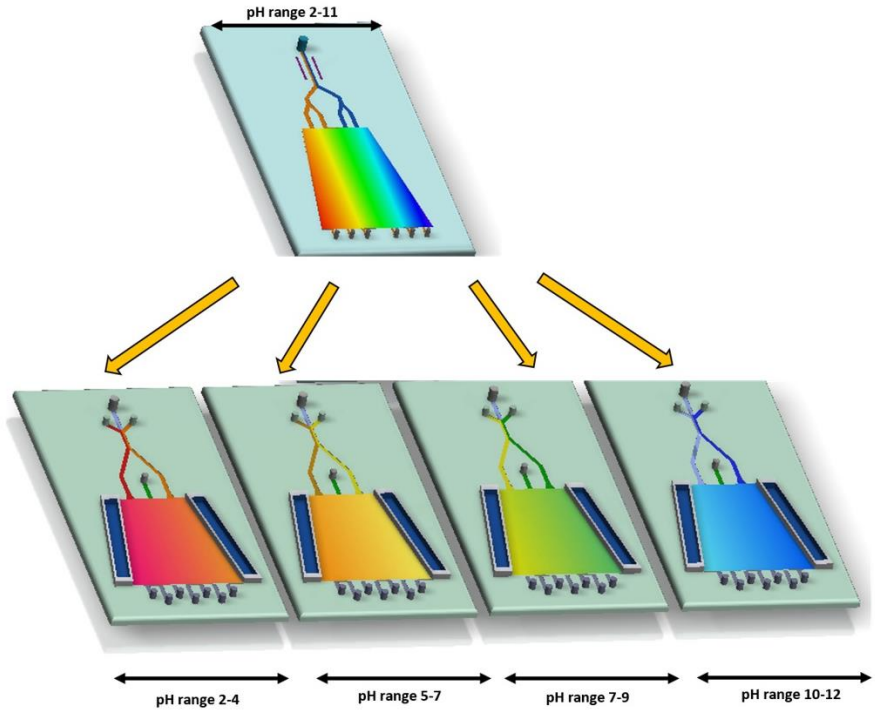

Supplementary Figure 18: Star topological configuration with pH gradient chip being the central node and different separation chips acting as connected nodes.

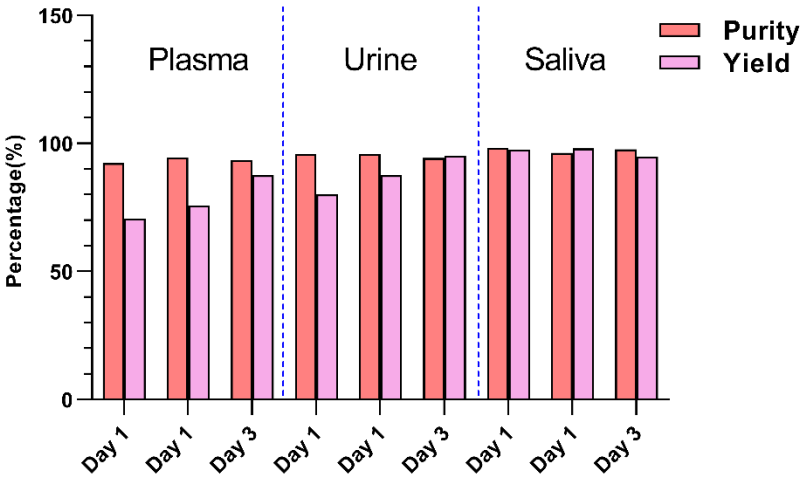

Supplementary Figure 19: The values of yield and purity for RNP fractionation in 3 different bio-fluids samples (plasma, urine, and saliva) demonstrate the inter-day and intra-day reproducibility of the CIF device.

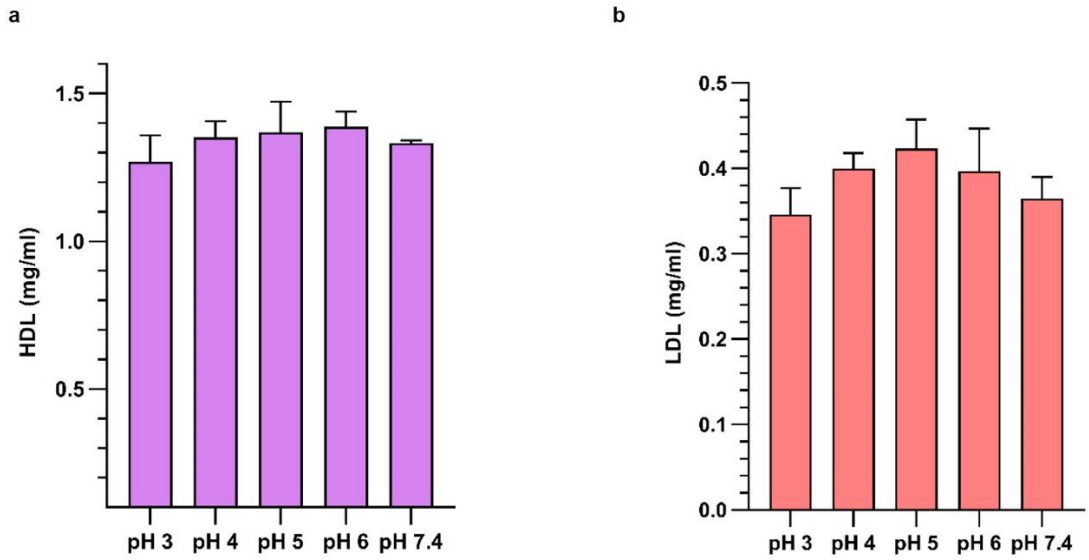

Supplementary Figure 20: Bradford assay results for a) HDL and b) LDL after incubation in different pH buffers at same concentration respectively.

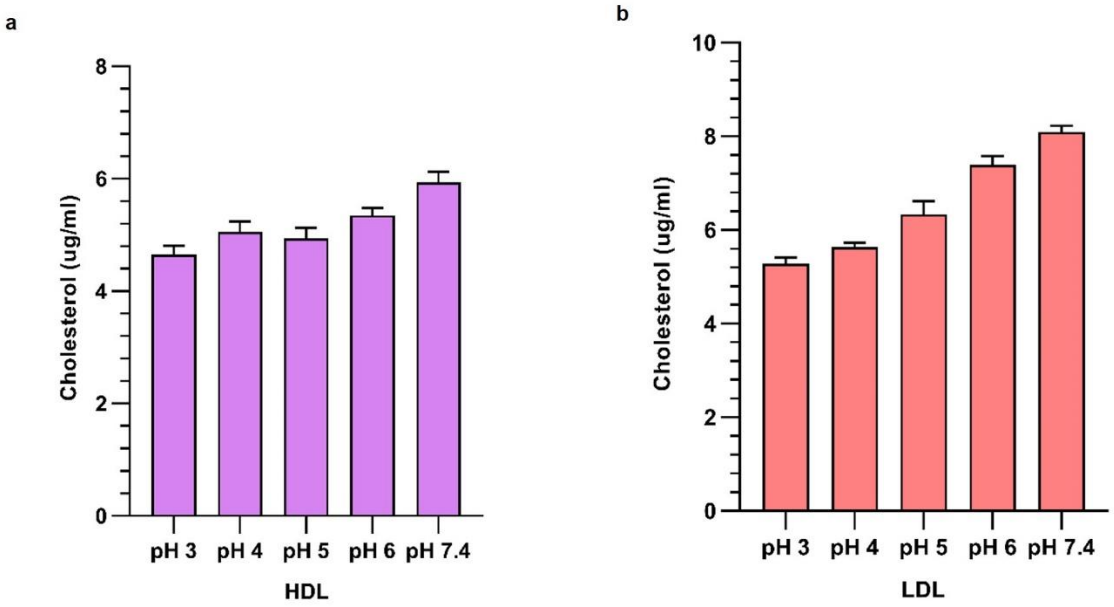

Supplementary Figure 21: Cholesterol assay results for a) HDL and b) LDL after incubation in different pH buffers at same concentration respectively.

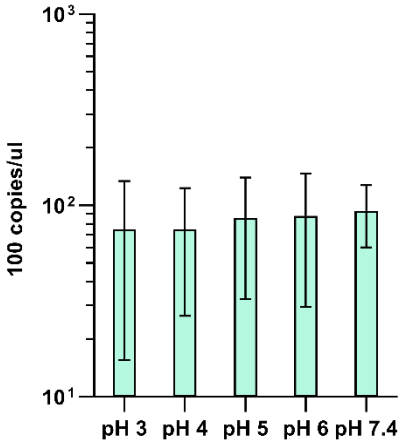

Supplementary Figure 22: RT-qPCR results of miR21 for RNP sample incubated in different pH buffers at same concentration.

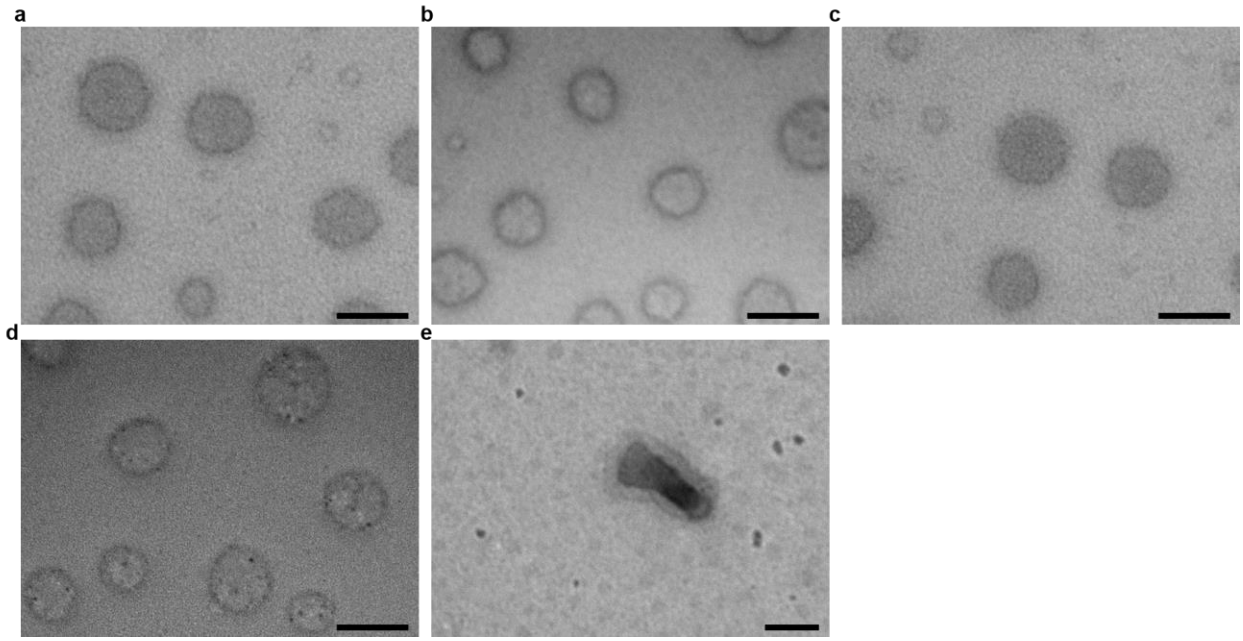

Supplementary Figure 23: TEM images of commercial EVs incubated in pH a) 7.4, b) 6, c) 5, d) 4 and e) 3. The scale bar is 100nm.

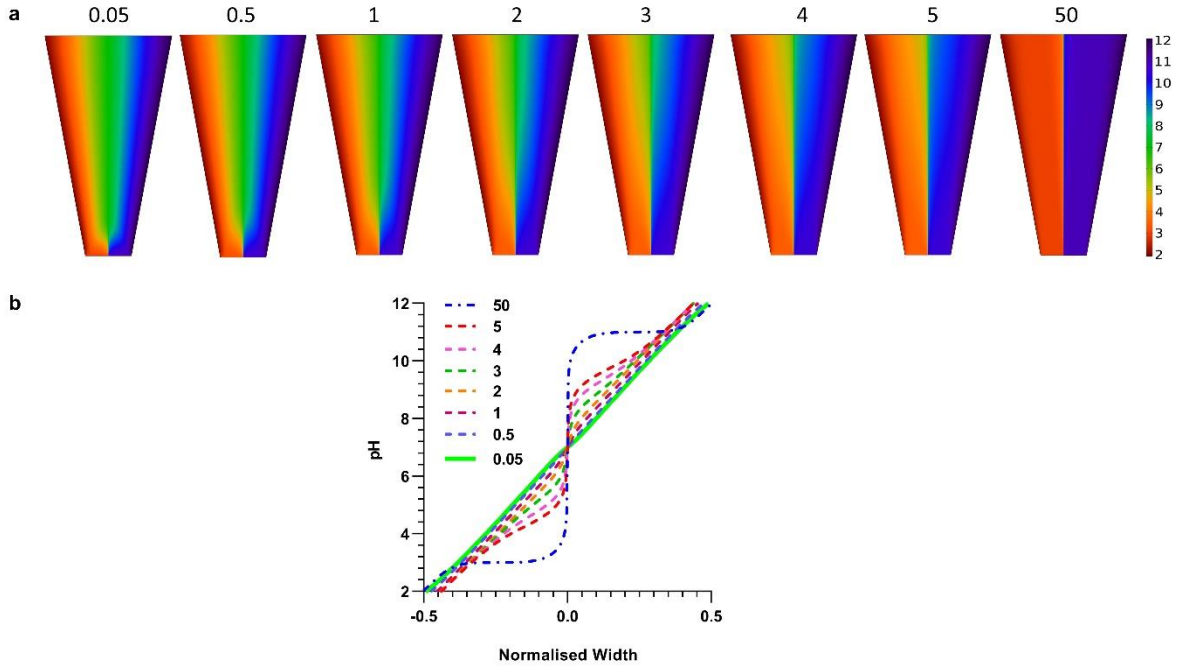

Supplementary Figure 24: a) Simulated pH profiles and their corresponding **b)** pH line plots for different rations of u_f/u_e (from 0.05 to 50) for a channel with dimensions of $W = 0.19L$.

Supplementary Note 1: pH Gradient Chip

The bipolar membrane (BiM), which is a sandwich between an anion-exchange membrane (AEM) and cation-exchange membrane (CEM), was assembled in such a way that one part of the membrane was exposed to an electrolyte reservoir and the other side to the microchannel. The two bipolar membranes (500-600 μm thick) were assembled on either side of the water transporting microchannel without any cross-membrane leakage (see Figure 1b and Supplementary Figure 1). Once filled with electrolyte, the BiM allows ion delivery into the microchannel. Under a reverse bias voltage across the two BiM reservoirs, an ion depletion zone of ~10 nm (the length of the Debye layer) appears at the AEM-CEM interface, such that the entire voltage drop occurs across this small layer[1]. This gives rise to a field of more than 10^6 V/cm, which is sufficient to split water into hydronium ions (H_3O^+) and hydroxide (OH^-) ions. The H_3O^+ and OH^- are electrophoretically driven through their respective membranes into the main channel where they are then partitioned, as shown in Supplementary Figure 1a. The high flow rate and their spatially segregated injection locations prevent extensive recombination of H_3O^+ and OH^- into the water at the injection site between the two BiMs. The amount of hydronium and hydroxide ions produced depends strongly on the applied DC bias as observed by the *I-V* characteristics of the BiM (Supplementary Figure 1c). The excessive ions generated by the field enhanced water dissociation at elevated voltage increase the local conductivity resulting in an increased current. The amount of water dissociation required under the applied field for obtaining a robust pH gradient was further optimized in a simple microfluidic device as shown in (Supplementary Figure 1a). Under a 30V reverse bias potential, and under an upstream flow rate of 12 ml/hour, a pH of 4 and 10 is collected at two outlets respectively. As the voltage is increased to 80 V a pH of 1 and 11 was collected at the two extreme outlets. At 90 V, a pH of 1 and 13 was collected from the two outlets (Supplementary Figure 1b). As the voltage increases further, the current also increased significantly and it was observed that a current beyond 1mA caused undesirable joule heating leading to bubble formation in the chip. Therefore, the optimized voltage bias and flow rate parameters were used subsequently.

This simple method does not produce any gaseous and harmful Faradaic reaction product contamination commonly observed in water electrolysis reactions. Also, as compared to other pH generation modules using either commercially available carrier ampholytes or injecting highly acidic and basic solutions through different inlets which ultimately dilutes the analyte, this method requires only a single microfluidic channel that can be bifurcated via splitter mixer channels to

produce a controllable pH gradient. Note that the outlet of the splitter-mixer has an angle of 45° at the inlet to the trapezoidal chamber to avoid the formation of vortices.

Supplementary Note 2: Theoretical explanation of pH profile

In the pH gradient generation chip, the segregated H_3O^+ and OH^- ions concentrate at the positive and negative electrodes, respectively, with a gradient *opposite* to their natural equilibrium Boltzmann distributions. Consequently, electroneutrality is maintained by the migrating buffer anions and cations (labelled A^- and B^+ respectively, in Figure 2a). Neglecting any Faradaic reaction of these inert buffer ions, they will equilibrate into their natural Boltzmann equilibria

$$C_{\pm} = C_{\pm}^{0} \exp\left(\mp \frac{|z|FE}{RT} y\right) \quad (1)$$

where $C_{\pm}$ denote the concentration of B^+ and A^- buffer ions respectively, $C_{\pm}^{0}$ is the respective reference ion concentration at the middle of the channel (y = 0) where the reference potential is zero, y is the transverse coordinate with the mid-channel as the origin, E is the constant transverse electric field in an electroneutral solution, F is Faraday constant, R is the universal gas constant, T is the temperature, and z is the valency of ions.

In tandem, to preserve local electroneutrality, the reactive H_3O^+ and OH^- ions adjust their (unequal) concentrations by rapid migration and association to form water to achieve the proper concentration for compensating the net charge due to the segregated buffer ion Boltzmann distributions (1). They hence take on the Boltzmann equilibrium concentrations of the buffer anion and cation, respectively, $C_{H_3O^+} = C_-$ and $C_{OH^-} = C_+$. These quasi-Boltzmann distributions of H_3O^+ and OH^- are opposite of their own natural Boltzmann distributions without reaction—they obey "negative" Boltzmann distributions. The recombination and dissociation kinetics, with unequal H_3O^+ and OH^- concentrations, are so fast that they do not reach transport equilibrium, described by their natural Boltzmann distribution, but rather reaction equilibrium to maintain electroneutrality by compensating the charge of the segregated buffer ions that are in Boltzmann distributions. The pH ($log_{10}(H_3O^+)$) profile is then specified by the mid-channel concentrations $C_{\pm}^{0}$. It is a linear spatial profile with anti-reflection symmetry across the midplane, for a constant transverse electric field in an electroneutral solution.

The above complete association theory can be improved by allowing for rapid but reversible equilibration of the water dissociation reaction,

$$2H_2O \rightleftharpoons H_3O^+ + OH^- \quad (2)$$

such that $K_w = C_{H_3O^+}C_{OH^-}$ everywhere (K_w is the auto-ionization constant of water), with the H_3O^+ and OH^- ions having concentrations that are inverse of each other—the acidic end is dominated by H_3O^+ and the basic end OH^-. At the middle of the channel, electroneutrality stipulates that this reciprocal relationship is transferred to buffer ions such that $C_+^0 C_-^0 = K_w$.

Away from the mid channel, however, local electroneutrality yields

$$\left(C_{H_3O^+} - C_{0H^-}\right) + \left(C_+ - C_-\right) = 0 \quad (3)$$

With Boltzmann distributions (1) for the buffer ions and the reciprocal relationships between H_3O^+ and OH^- ions and between the midchannel buffer ion concentrations, with constant K_w, this electroneutrality condition hence specify the hydronium ion concentration and the pH at every position. The distributions are only dependent on the midchannel anion concentration C_-^0 and the local transverse field *E*. This universal distribution applies to the pH generation chip but is also true for the separation chip when a subsection of the pH profile is extracted from the pH generation channel. The only difference is reference buffer anion concentration C_-^0, which is a function of the extracted segment from the upstream generation chip. Hence, the linear pH profile corresponding to $C_{H_3O^+} = C_- = C_-^0 exp\left(\frac{|z|FE}{RT}y\right)$ is obeyed everywhere across both channels. The trapezoidal shape of the separation chip produces an electric field *E* that decreases linearly downstream and the constant pH contours should be linear radial loci in the channel.

The universal "negative" Boltzmann distribution of hydronium ions, with only the mid-channel reference concentration specified by the feeds, implies that any linear section of the pH profile in the upstream chip can be stretched to any length scale in the downstream chip, depending only on the electric field *E* or the width of the trapezoidal microchannel when a constant potential is applied at the two channel sides. This flexibility allows us to tune the pH range and spatial resolution in the separation chip to achieve high-resolution isoelectric separation.

Supplementary Note 3: Mathematical calculation of linear pH profile in both trapezoidal and straight channels

The linear pH profile in the range $[pH_{start}, pH_{end}]$ straight channel and trapezoidal channel in dimensionless form should appear as follows

$$pH_{straight} = pH_{start} + \Delta pH_{straight} * \left(\frac{x}{w}\right) \quad (4)$$

$$pH_{trapezoidal} = pH_{start} + \Delta pH_{trapezoidal} * \left(\frac{x}{w+2*l*\tan(\theta)}\right) \quad (5)$$

Since the dimensionless profile is same for both the cases:

$$pH_{trapezoidal} = pH_{straight}$$

$$\Delta pH_{trapezoidal} * \left(\frac{x}{w+2*l*\tan(\theta)}\right) = \Delta pH_{straight} * \left(\frac{x}{w}\right)$$

$$\frac{\Delta pH_{trapezoidal}}{\Delta pH_{straight}} = \frac{w+2*l*\tan(\theta)}{w}$$

$$\frac{\Delta pH_{trapezoidal} - \Delta pH_{straight}}{\Delta pH_{straight}} = \frac{2*l*\tan(\theta)}{w} \quad (6)$$

For the pH generation chip $w = 20.2\,mm$ and $l = 26.57\,mm$ and $\tan(\theta) = 10^0$ and the percentage increase in the pH gradient resolution in trapezoidal geometry is 63.07% as compared to the straight geometry.

Supplementary Note 4: Insensitivity of linear pH gradient to flow

Let the inlet fluid velocity be u_f and u_e be the orthogonal fluid and electrophoretic velocities. To obtain a linear pH gradient during the fluid residence time inside the trapezoidal channel, the electrophoretic time across the channel t_e must be smaller than the fluid residence time t_f,

$t_e < t_{f,}$

or

$$\frac{W}{u_e} < \frac{L}{2u_f},$$

where *L* and *W* are the length and half-width of the channel at *L*/2, which is our chosen location for a stable pH gradient to be established. We can see that the corresponding relationship between the fluid and electrophoretic velocities is

$$u_f < \frac{L}{2W} * u_e.$$

If we substitute in the relationship for the electrophoretic drift relative to the electric field E and mobility μ_e, this becomes

$$u_f < \frac{L}{2W} * \mu_e E.$$

Using Einstein-Stokes relationship between diffusivity and mobility, we obtain the upper bound on the flow velocity

$$u_f < \frac{L}{2W} * \frac{zFD}{RT} E$$

Simulations of pH profiles for different u_f/u_e ratios are shown in Supplementary Figures 24 for a specific case of $W = 0.19L$. Notably, the inlet velocity does not influence the formation of a linear pH profile but instead just changes the downstream location where the linear pH gradient is established after initial pH transients. Separation at the middle of the channel is indeed observed when u_f/u_e > 2.66. At very high ratios (> 5), the fluidic residence time becomes very small which inhibits any effect of the electric field on the pH profile.

Supplementary Note 5: Optimized conditions for separating HDL and LDL

For separation of target ampholytes such as HDL and LDL, two key optimal conditions are needed: a pH range for performing pure separation and the applied voltage bias to deflect the nanocarriers prior to their residence time in the chip[2]. The optimum condition for the latter was obtained from the charged latex nanoparticle deflection experiments. Hence, the ensuing set of experiments optimized the pH range required to sufficiently separate HDL and LDL. Initially, the pH range [1-13] obtained from the pH generation chip was used to test the isoelectric focusing of the labelled nanocarriers individually (Supplementary Figure 5a). For LDL (Supplementary Figure 5b), the particles were deflected towards their respective pIs as shown from the snapshots at voltage bias of 100V and 150V. Similarly, for HDL, the same behavior was observed (Supplementary Figure 5c). However, a mixture of these ampholytes cannot be separated since both the labelled ampholytes were collected from the same outlet. Therefore, these experiments suggested to lower

the pH range from 1-13 to 3-6 for generating a high-resolution pH gradient for efficient recovery of these lipoproteins.

Supplementary Note 6: **Optimized conditions for carboxylated and aminated latex particles in the separation chip**

In order to test and optimize the performance of the separation chip, fluorescently labeled carboxylated and aminated latex nanoparticles (50 nm) were initially selected as a sample analyte. pH streams of 2 and 10 from two outlets coming from the pH generation chip was fed into the pH inlets of the separation chip whereas the labeled nanoparticles (0.25% solids (w/v)) were injected into the sample inlet of the separation chip (Supplementary Figure 3). After selecting a pH flow rate of 12 ml/hour for high throughput application, the potential applied across the chip was optimized. When a voltage bias of 100 V was applied across the separation chip, a small deflection in the carboxylated stream was observed with a broad focused peak (Supplementary Figure 3a). However, for aminated particles, the defection was minimal. As the voltage bias was increased to 150 V, a decent focusing of the particles was observed (Supplementary Figure 3b). It should be noted that in carboxylated nanoparticle separation: two focused bands were observed which should include the carboxylated particles as well as the charged fluorescent impurity (mostly fluorescent dyes). It is likely that this method can easily be extended towards the purification of nanoparticles from labeled dyes/impurities.

Supplementary Note 7: Optimized conditions for separating RNP and HDL

After successfully separating the LLPs namely HDL and LDL at a high throughput of 3 ml/hour, the CIF platform was then optimized for the separation of a RNP and LLP (HDL as the model LLP). In the previous study of HDL and LDL separation, we obtained the optimum voltage bias required to deflect the LLPs to their pIs prior to their residence time in the chip. We used the same voltage bias of 150 V in initial experiments for the separation of a mixture of HDL and RNP (Supplementary Figure 7). A pH range of 2-10 (Supplementary Figure 7a) was selected to be transferred from the pH generation chip to the separation chip as the pIs of HDL and RNP lie on the acidic and basic side respectively. A series of snapshots of the experimental images

(Supplementary Figure 7b) show that the nanocarriers mixture is being successfully deflected towards their respective pIs. However, the separation of these nanocarriers in the chip was not very efficient and two broad separation bands were observed as shown in the zoomed in images with the onset of separation skewed towards the acidic front. This issue was addressed by transferring a lower pH range 2-8 from the pH generation chip and increasing the voltage bias to 200 V to obtain a fine separation between RNP and HDL as shown in Supplementary Figure 8.

Supplementary Note 8: Use of *auto-CIF analyzer* for 3D printed CIF microfluidic chip

The 3D printed CIF chip is printed with HTL resin (the most transparent resin currently available in the market for the 3D-printer that can print our CIF geometry) has an inherent background from the photo-polymerized resin, which can skew visual pH measurements. Hence, the auto-CIF analyzer was a necessary tool to identify the outlets for effective pH range transfer to the 3D printed separation chip. The workflow is the same as described previously for xurography-based chips. For the image segmentation module, the machine learning classifier was trained on images from 3D printed chips and the confusion matrix of the testing data is shown in Figure 4b. The classifier yielded an accuracy of 97.93%, sensitivity of 91.57%, and specificity of 98.91%[3]. Furthermore, the segmented area predicted by machine learning is in excellent agreement with the area of the ROI calculated manually as shown in Figure 4c. Owing to the background of the 3D printed chip, sequential digital images were taken by injecting different known pH solutions into the chip (Figure 4f). By using all the normalized mean RGB values as independent variable vectors, a good correlation with its pH value was obtained with a MSE of 0.573 (Figure 4h). The error was even further reduced by dividing the data into acidic (pH = [2-6]) and basic pH values (pH = [7-11]) yielding a pH MSE of 0.175 and 0.468, respectively (Figure 4h). Subsequently, a pH surface plot was generated for a sample segmented test image of the 3D printed device as shown in Figure 4j. The *auto-CIF analyzer* platform can conceptually be further used for other applications whose output corresponds to a digital image comprising of a gradient of colors such as concentration gradient generation, colorimetric ELISA[4], and similar tests.

Supplementary Note 9: Image Segmentation Module and pH Detection Module of *auto-CIF analyzer*

Semantic segmentation classifier using ilastik was developed for each chip type: polycarbonate-based chip and 3D printed chip. Two classes, ROI and background, were made for the binary classification. The classifier extracted a total of 37 features which includes color/intensity, edge, and texture. The interactive GUI of ilastik was used to manually label pixels, monitor the output, and calibrate the labels with further annotations until acceptable segmentation was obtained for all the training images using the default random forest classifier with 100 trees. After successfully training the classifier manually using their interactive GUI, the test images were batch processed to generate the labelled binary images. For the xurography-based chip, 29 images were trained, and 136 test images were batch processed whereas for the 3D printed chip, 21 images were trained, and 41 test images were batch processed to obtain segmentation masks. The segmentation mask was then cleaned to fill holes and remove noisy pixels by area filter. The original colorimetric test images were then exported to Matlab and its image labeler app was used to generate ground truth data for all the test images. The label corresponding to each pixel of the ground truth data and the predicted binary image was then compared across all test images for the respective chip type to calculate True Positive (TP), True Negative (TN), False Positive (FP) and False Negative (FN). These values are shown in tabular format (Supplementary Figure 17) and were used to make the confusion matrix (Figure 4b and 4d). Furthermore, other semantic segmentation metrics were calculated as defined as[70]:

$$\text{Accuracy} = \frac{(\text{TP}+\text{TN})}{(\text{TP}+\text{TN}+\text{FP}+\text{FN})} ;$$

$$\text{Sensitivity} = \frac{\text{TP}}{(\text{TP}+\text{FN})} ;$$

$$\text{Sensitivity} = \frac{\text{TP}}{(\text{TP}+\text{FP})} .$$

In the pH detection module, two different calibration curves were generated depending upon the chip type. For the transparent xurography-based chip, first, an image was taken by a smartphone of the pH reference chart of Hydrion pH Indicator Solution (Microessential lab, Cat. UI-100). The histograms of the RGB values corresponding to each pH [1-11] are shown in Supplementary Figure 15. Mean RGB values were then calculated corresponding to each pH value. To further minimize the effect of uneven illumination from the constant illumination source on the mean RGB values, they were additionally normalized to obtain $\widehat{\text{R}}$, $\widehat{\text{G}}$, and $\widehat{\text{B}}$ values such that

$\hat{R} = \frac{\mathrm{R}}{\mathrm{R+G+B}}$;

$\hat{G} = \frac{\mathrm{G}}{\mathrm{R+G+B}}$;

$\hat{B} = \frac{\mathrm{B}}{\mathrm{R+G+B}}$.

A multivariate linear regression model was developed based on the $\hat{\mathrm{R}}\hat{\mathrm{G}}\hat{\mathrm{B}}$ values using

$pH = \alpha\hat{R} + \beta\hat{G} + \gamma\hat{B}$,

where α, β, and γ are fitting coefficients.

In the case of the 3D printed chip, owing to the presence of large background, a new calibration curve was generated by taking a sequence of images by injecting different known pH solutions into the chip. The histograms of the RGB values corresponding to each pH [2 – 11] are shown in Supplementary Figure 16. Once the coefficients were obtained for each chip type, the linear formula was used to calculate the pH corresponding to each pixel in the experimental image. The segmented image of the ROI was multiplied by the original colorimetric image, and a pH surface plot across the ROI was generated.

Supplementary Note 10: On-chip gel electrophoresis and gel electrophoresis experimental details

On-Chip Gel Electrophoresis: A 5 mm × 60 mm rectangular through hole was cut in the middle of a 40 mm × 80 mm acrylic sheet (8560K188, Mcmaster Carr, USA) using a micro milling machine (Roland monoFab SRM-20, Roland DG, USA). The sheet is then sandwiched between two 40 mm × 80 mm double-sided Kapton tape (PPTDE-3, Katontape.com), which were cut using a plotter cutter (Graphtec Pro FC7000). The upper Kapton tape contained two holes for inlet as well as outlet and another hole which acts as a microwell for injecting the sample. Two plastic cuvettes acting as fluid reservoirs (97000-590, VWR, USA) were cut and glued on top of the top sheet of Kapton tape with the holes being at the centre of the cuvettes (Supplementary Figure 4). The fluid reservoirs were filled with 1× PBS buffer. 2% of heated agarose solution was injected into the chip, cooled at 4°C for half an hour and a portion of gel in the microwell is cut. Finally, 5 µl of the sample was injected into the microwell and a voltage bias of 100V was applied[69]. The

chip was then placed on a Dark Reader blue transilluminator (DR89 Mid-Size Transilluminator, Clare Chemical Research, USA) for fluorescence image acquisition.

Gel Electrophoresis: Gel electrophoresis of tagged HDL, LDL, RNP and commercial EVs was performed in 2% agarose gel made in TAE buffer in the Mini-Sub Cell GT Cell (Bio-Rad, USA) for 30 mins at 100 V. Fluorescence image acquisition was done under a Dark Reader blue transilluminator (DR89 Mid-Size Transilluminator, Clare Chemical Research, USA).

Supplementary References:

(1) Cheng, L.-J.; Chang, H.-C. Microscale PH Regulation by Splitting Water. *Biomicrofluidics* **2011**, *5* (4), 046502. https://doi.org/10.1063/1.3657928.
(2) Jang, W.; Shim, J.; Lee, D.-Y.; Dutta, P.; Kim, J.-R.; Cho, K.-H. Rapid Detection of Dysfunctional High-Density Lipoproteins Using Isoelectric Focusing-Based Microfluidic Device to Diagnose Senescence-Related Disease. *Electrophoresis* **2011**, *32* (23), 3415–3423. https://doi.org/10.1002/elps.201100361.
(3) Thanh, D. N. H.; Prasath, V. B. S.; Hieu, L. M.; Hien, N. N. Melanoma Skin Cancer Detection Method Based on Adaptive Principal Curvature, Colour Normalisation and Feature Extraction with the ABCD Rule. *J. Digit. Imaging* **2020**, *33* (3), 574–585. https://doi.org/10.1007/s10278-019-00316-x.
(4) Anastassopoulou, C.; Tsakris, A.; Patrinos, G. P.; Manoussopoulos, Y. Pixel-Based Machine Learning and Image Reconstitution for Dot-ELISA Pathogen Diagnosis in Biological Samples. *Front. Microbiol.* **2021**, *12*, 347. https://doi.org/10.3389/fmicb.2021.562199.